JSR Publications

Available Online

J. Sci. Res. **12** (4), 555-567 (2020)

JOURNAL OF SCIENTIFIC RESEARCH

www.banglajol.info/index.php/JSR

Investigation of Magnetic and Optical Properties of Mn-Doped SnO_2 at Different Annealing Temperatures

Sunaina, A. Sharma, P. Sharma*

Department of Physics, School of Basic and Applied Sciences, Maharaja Agrasen University, Solan, H.P, India

Received 20 March 2020, accepted in final revised form 9 June 2020

Abstract

In this paper, a systematic investigation has been done to study the effect of variation in annealing temperature on magnetic and optical properties of Mn-doped SnO_2. Co-precipitation technique has been used to synthesize $Sn_{1-x}Mn_xO_2$ samples with low Mn concentration (2 %). Pristine SnO_2 is sintered at 350 °C. Mn-doped SnO_2 samples are sintered at 350, 450, 550 and 650 °C. The structures of tetragonal rutile of SnO_2 and Mn-doped SnO_2 have been confirmed by the XRD pattern. Typical ferromagnetic ordering has been observed for Mn-doped SnO_2 samples annealed at different temperatures. However, on increasing the annealing temperature saturation magnetization as well as the coercive field decreases, indicating a crucial phase transformation from ferromagnetism to paramagnetism. UV-Vis spectroscopy shows increase in absorbance and a slight shift in the absorption edge with Mn-doping at increasing annealing temperature indicating shifting of absorption peak towards higher wavelength. Tauc's plot has been used to find the optical band gap (E_g).

Keywords: Annealing temperature; Co-precipitation; X-ray diffraction; Energy band gap.

© 2020 JSR Publications. ISSN: 2070-0237 (Print); 2070-0245 (Online). All rights reserved.
doi: http://dx.doi.org/10.3329/jsr.v12i4.46052 J. Sci. Res. **12** (4), 555-567 (2020)

1. Introduction

Recently, nanoscale materials have gained enormous interest due to their interesting multifunctional properties which can be harnessed at nanometric scale. Among various nanomaterials, diluted magnetic semiconductors (DMS) have attracted attention owing to their unique property of room temperature ferromagnetism (RTFM). These materials have gained importance since their spin degree of freedom and charge carrier properties can be coupled together to tune them for future spintronic applications, thus for fabrication of multifunctional devices [1,2]. Investigations have been extensively focussed on various II-VI semiconducting oxide DMS materials like ZnO, TiO_2, CuO, SnO_2 etc. [3]. In particular, a wide band gap of 3.6 eV at room temperature of the n-type SnO_2 has made it a promising material for a wide variety of optoelectronic devices [4,5] gas sensors [6], transparent conducting electrodes [7], catalyst supports [8] and spintronics [9]. Its high optical transparency, good electrical conductivity, low defect density and chemical

*Corresponding author: royprianka04@gmail.com

sensitivity properties can be harnessed for many practical applications like solar cells, light emitting diodes, lithium ion batteries, gas sensing and field effect transistors etc. [10-12].

The multifunctionality of SnO_2 can be improved extensively by impurity doping with transition materials (TM) like Fe, Co, Ni, Cu, Mn etc. Ahmed *et al*. [13] studied that varying concentration of TM doping can alter the room temperature electrical and dielectric properties. In similar manner, it has been observed by many research groups that room temperature ferromagnetism, structural and optical properties of SnO_2 can be tuned by doping it with transition metals [14-20]. Optoelectronic properties like band gap and photoluminescence can also be tuned by impurity doping in SnO_2 [21]. Spin induced RTFM was predicted for doped SnO_2 with TMs V, Fe, Ni, Co and Cr by first principle study and experimentally as well [22-24]. Coey *et al.* have reported decrease in magnetization of SnO_2 doped with Fe, Mn, Co with increasing concentration due to antiferromagnetic super exchange interaction between TM and oxygen ions [3]. Liu *et al.* observed relationship between structural and magnetic properties of Co-doped SnO_2 nanoparticles [25]. Fitzgerald *et al.* reported the Curie temperature of Mn- and Co-doped SnO_2 at 340 K and 360 K [26]. Ogale *et al.* observed that SnO_2 doped with Co showed high temperature ferromagnetism as well as giant magnetic resonance [27]. Various groups remarked about the effect of Ni doping in SnO_2 for various spintronic applications [28]. Researchers have shown that several dopants (Co, Fe, Cu) can lead to an increase in surface area of SnO_2 by reducing grain size and crystallinity [29]. It can be concluded that doping proves to be an impressive technique in controlling the electronic, spintronic and optical properties of semiconductors [30]. This approach brings about structural and compositional alterations in semiconductors by changing their particle or grain size. Recently, Mn doping with variation in concentration has been much emphasized since it can tailor the structure, morphology, crystallinity and thereby chemical properties of SnO_2 [31,32]. Mn ions proved to be a good candidate for replacing Sn ions in lattice of SnO_2 due to its large equilibrium solubility and nearly same ionic radii as compared to Sn^{4+} ion for substitution, which can thereby provide increased spins and carriers for spintronic applications. By doping Mn the electronic configuration of SnO_2 modulates and gives rise to a huge amount of oxygen vacancies [33]. Mn ions exhibit giant sp-d exchange coupling and interesting properties like non-linear band splitting along with spin polarized bands [34]. This ability of tuning of position of Mn optical bands has stimulated great interest in the magneto-optical properties of Mn-doped SnO_2.

Till now, much concern has remained on the introduction of Mn ions into the SnO_2 lattice with the variation in Mn concentration and synthesis techniques adopted [15,18,31-34]. However, not much study has been done on the investigation of effect of annealing temperature on the growth of bulk materials of nano-sized dimensions. In the present work, we have chemically synthesized Mn-doped SnO_2 powders by co-precipitation technique and annealed at different temperatures. A detailed study has been done to investigate various reasons for the origin of RTFM and change in the band positions in Mn-doped SnO_2 powders annealed at different temperatures.

2. Experimental

Pristine and Mn-doped SnO_2 nanoparticles have been synthesized by co-precipitation technique. Appropriate amounts of $SnCl_2.2H_2O$ and $MnCl_2.4H_2O$ in proportion of 50:1 were taken and dissolved in 100 mL of deoxygenated distilled water. The sol was prepared by stirring the solution for 2 h at 80 °C and then 50 mL of NH_4OH was mixed drop-wise under magnetic stirring to get the precipitates. The solution was then stirred for 15 min. The precipitates were continuously washed at least 2-3 times and then filtered, and dried in air for several hr. The dried precipitates were then annealed for 2 h at different temperatures between 350 to 650 °C to obtain the final Mn-doped SnO_2 powder. The samples were then characterized by X-ray diffraction (XRD), SEM and EDAX for structural, morphological and compositional investigations. The magnetic investigations of the Mn-doped SnO_2 powders were carried out with Vibrating Sample Magnetometer (VSM). UV-Vis-NIR spectroscopy was done to study the proper Mn ion substitution in SnO_2 lattice.

3. Results and Discussion

3.1. *Structural investigations*

Pristine SnO_2 and Mn-doped SnO_2 powders have been analyzed for the crystal structure and phase purity by the X-ray diffraction patterns. Fig. 1 shows the XRD pattern of pristine SnO_2 annealed at 350°C, Mn-doped SnO_2 samples annealed at 350°, 450°, 550°and 650°C. Peaks have been observed corresponding to the (110), (101), (200), (211), (220), (002), (112) and (301) planes and compared with the XRD pattern of pristine SnO_2 on the basis of JCPDS file no. 88-0287 [35]. The prominent peaks indexed correspond to the tetragonal rutile structure of pristine SnO_2 and Mn-doped SnO_2. No additional phases like orthorhombic SnO_2, metallic Mn or other SnO-based phases are observed in the XRD patterns. Hence, it can be concluded that the transition metal ions are successfully substituted at the Sn site and Mn impurities do not affect the tetragonal structure of SnO_2. From the XRD patterns, it is also observed that with increasing annealing temperature, the intensities of the XRD peak of the Mn-doped SnO_2 samples increases. This shows that though the crystallite size decreases with introduction of Mn dopant but with increasing annealing temperature the crystallite size increases. The reason is that with Mn doping the oxygen vacancies increases because of smaller ionic radius of Mn^{3+} ion (0.65 Å) in comparison to Sn^{4+} ion (0.69Å) which inhibits the growth of the crystal grains due to the presence of Mn ions in SnO_2. Hence, the crystallite size decreases due to disturbance in the long range crystallographic ordering. But annealing the samples at higher temperature improves the crystallinity of the sample. With increasing annealing temperature, sharpness of the diffraction peaks intensifies and broadening of peak goes on decreasing. A broad diffraction peak indicates smaller particle size but with increase annealing temperature, broadening decreases enhancing the particle size.

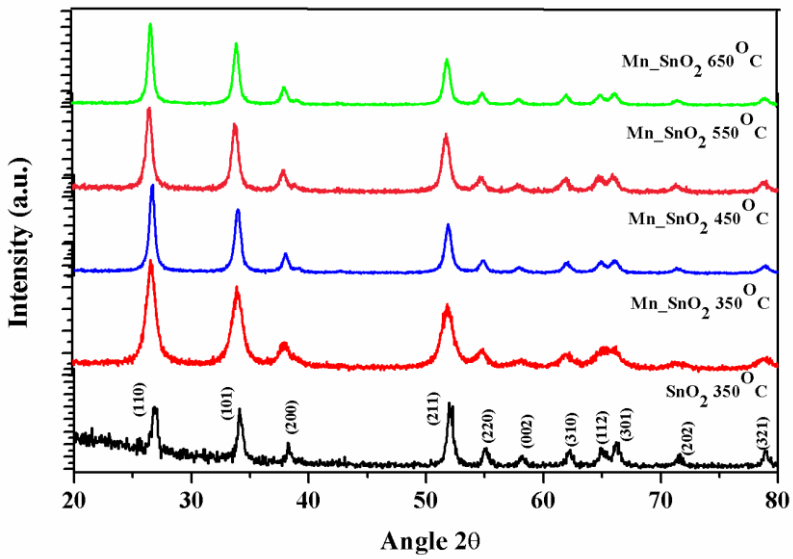

Fig. 1. XRD patterns of Mn-doped SnO_2 annealed between 350 °C to 650 °C and pristine SnO_2 annealed at 350 °C.

This is because as the annealing temperature increases, the lattice of SnO_2 is modified since the Sn^{4+} ions are replaced by Mn^{3+} ions which increases the intensity of peaks in diffraction patterns. This leads to more disorders in the crystal lattice due to change of the interstitial sites of Sn^{4+} ions [36]. Thus, doping Mn on SnO_2 reduces the crystallite size but annealing at higher temperatures increases the crystallite size and hence improves the crystallinity of the material [37]. The average crystallite size (D) has been determined by Scherrer's formula [38] using the diffraction peaks (110) and (101)

$$D = \frac{k\lambda}{\beta \cos\theta} \tag{1}$$

In this Eq. (1), $k=0.9$, λ represent the wavelength of the X-ray radiation, β is the full width at half maximum of the diffraction peak (in radians) and θ the Bragg diffraction angle at full width half maximum (FWHM) of the diffraction peak.

For tetragonal system, the *d*-spacing (d_{hkl}) and lattice constants, *'a'* and *'c'*, are calculated using Eq. (2)

$$\frac{1}{d^2} = \frac{h^2 + k^2}{a^2} + \frac{l^2}{c^2} \tag{2}$$

where *'d'* is the interplanar distance, *(hkl)* are the miller indices and *'a'* and *'c'* are the lattice constants.

In Table 1, we present the variation of the crystallite size (*D*), FWHM (β), lattice parameters *'a'* and *'c'* with variation in annealing temperature. The given parameters in Table 1 are in accordance with the conclusions from the XRD patterns. It is clear that the

full width at half maxima (FWHM) values change with annealing. The FWHM of 2θ are related to the crystalline quality of the bulk samples. For pristine SnO_2 annealed at 350 °C, the FWHM value is (0.0041). With Mn doping the FWHM value increases at 350 °C (0.0073), indicates smaller crystallite size at 350 °C. With increase in annealing temperature from 350 to 650 °C, the FWHM values decreases from 0.0073 to 0.0038. At 650 °C, the sample shows sharper and intense peak with a smaller FWHM. The lattice parameters also show the same trend. For Mn-doped SnO_2 sample annealed at 350 °C, the lattice parameters '*a*' and '*c*' increases compared to pristine SnO_2 but decreases with increasing annealing temperature. Both the FWHM and lattice parameter values indicate increase in particle size and therefore crystallinity with increase annealing temperature.

Table 1. XRD Data of Pristine SnO_2 sample and Mn-doped SnO_2 samples at different annealing temperature.

Sample name	Annealing temp (°C)	Crystallite size (nm)	FWHM	A (Å)	c (Å)
Pristine SnO_2	350	35.00	0.0041	4.68	3.15
Mn_SnO_2	350	19.52	0.0073	4.75	3.22
Mn_SnO^2	450	29.48	0.0049	4.74	3.20
Mn_SnO_2	550	33.00	0.0044	4.73	3.18
Mn_SnO_2	650	34.50	0.0038	4.72	3.16

Fig. 2 illustrates the surface morphology of nanocrystalline Mn-doped SnO_2 powders annealed at 350, 450, 550 and 650 °C. It has been observed that particles are found to aggregate more with increasing annealing temperature. This might be due to the reason that the surface defects in the SnO_2 lattice increases with increase in temperature. This leads to decline in the number of nucleation centres due to random diffusion of Mn ions into the SnO_2 lattice, thereby leading to surface redistribution of grains and increasing the grain growth.

The chemical and compositional formation of Mn-doped SnO_2 samples are examined by EDX analysis. Fig. 3 shows the EDX spectrum of Mn-doped SnO_2 samples annealed at 350, 450, 550 and 650 °C. The spectrum confirms the presence of the constituents i.e., Sn, O and Mn. The EDX spectra show the presence of Mn ions thereby confirming the successful incorporation of Mn ions into the host lattice of SnO_2. The sharp and consistently increasing peaks of Sn and Mn with increasing annealing temperature, confirms the increase in crystallinity of the samples [39].

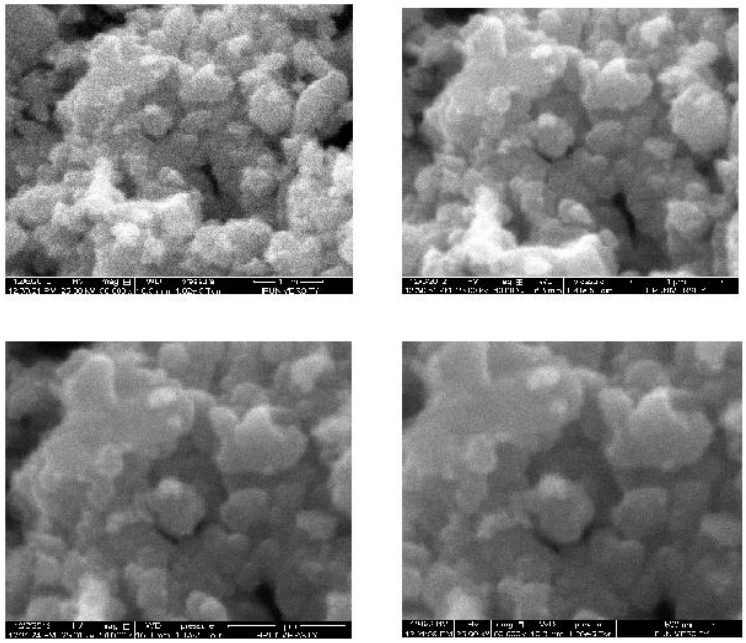

Fig. 2. SEM morphology images for nanocrystalline Mn-doped SnO_2 powders annealed 350, 450, 550 and 650 °C.

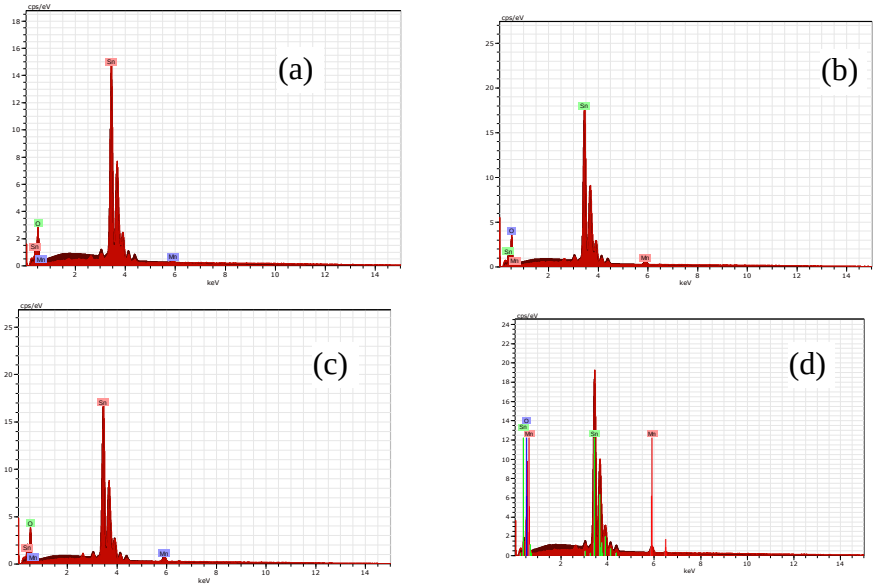

Fig. 3. EDX images for nanocrystalline Mn-doped SnO_2 powders annealed at (a) 350 °C, (b) 450 °C, (c) 550 °C and (d) 650 °C.

3.2. *Magnetic investigation*

Magnetic measurements for Mn-doped SnO_2 have been done at room temperature by VSM in varying magnetic field. Fig. 4 shows the magnetization vs. magnetic field (MH) curve at room temperature for Mn-doped SnO_2 samples annealed at temperatures 350, 450, 550, and 650 °C. Pristine SnO_2 exhibits a diamagnetic behaviour at 350 °C. The diamagnetic behaviour of SnO_2 sample at low annealing temperature maybe because of distortion created in the lattice structure of SnO_2 due to low diffusion of oxygen vacancies into the tin lattice. This distortion in lattice structure decreases the overlapping of bound magnetic polarons (BMP's) which leads to weak ferromagnetic interaction. It is further suppressed by the diamagnetic ordering which is the intrinsic property of SnO_2 [1]. On increasing the annealing temperature, slight ferromagnetic ordering maybe introduced or the system may show paramagnetic behaviour. Typical ferromagnetic ordering (magnetic saturation) has been observed for Mn-doped SnO_2 samples annealed at 350, 450, 550 and 650 °C. However, on increasing the annealing temperature, saturation magnetization decreases at high magnetic field. Origin of RTFM has always remained a puzzling question for DMS materials. It has been predicted that exchange interaction between spin states of Mn^{4+}, Mn^{3+} and Sn^{4+}cations are responsible for RTFM in Mn-doped SnO_2 samples. Strong ferromagnetic coupling is experienced by the Mn ions into the SnO_2 lattice. This type of coupling arises due to exchange of F-centres of doped-ion of transition metal and the oxygen vacancies present in SnO_2 lattice. At the sites of oxygen vacancies, one electron of transition metal gets trapped and creates the F-centres. The F-centre electron then couples with neighbouring d-shell orbital of Mn^{3+} ions. According to Pauli's exclusion principle and Hund's rule, in order to achieve ferromagnetic ordering, parallel spin orientation is observed between the trapped electrons and neighbouring Mn ions. Another reason ascribed to ferromagnetic ordering of Mn-doped SnO_2 may be due to overlapping of BMP's.

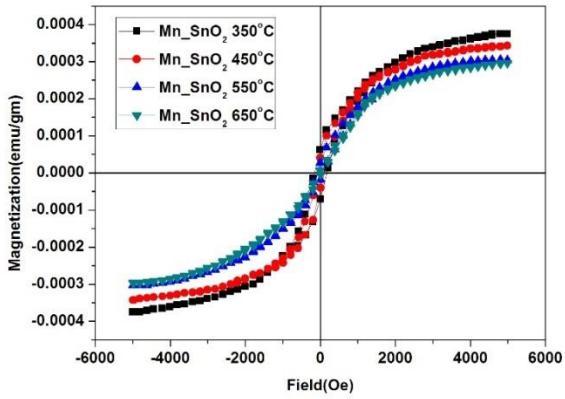

Fig. 4. M-H magnetization curves for nanocrystalline Mn-doped SnO_2 samples annealed at 350, 450, 550 and 650 ^oC.

These BMP's are formed when bound electrons at oxygen vacancy sites coupled with Mn ions spins incorporated in SnO_2 lattice. The ferromagnetic coupling is also strongly influenced by the variation in structural parameters like interatomic distances (lattice parameters). The calculated magnetic parameters are presented in Table 2 which shows that the saturation magnetization, coercivity and remnant magnetization decreases as the particle size increases with increase the annealing temperature.

Table 2. Magnetic Parameters of Mn-doped SnO_2samples at different annealing temperatures.

Sample name	Crystallite size (nm)	Saturation magnetization (M_s) emu/gm	Coercivity (H_c) Oe	Remnant magnetization (M_r) emu/gm
Mn_SnO_2_350 °C	19.52	3.75×10^{-4}	173	6.00×10^{-5}
Mn_SnO_2_450 °C	29.48	3.43×10^{-4}	117	3.75×10^{-5}
Mn_SnO_2_550 °C	33.00	3.04×10^{-4}	77	2.50×10^{-5}
Mn_SnO_2_650 °C	34.50	2.80×10^{-4}	35	5.00×10^{-6}

At higher magnetic field, the coupling due to antiferromagnetic exchange interaction enhances which decreases the saturation magnetization level [40].

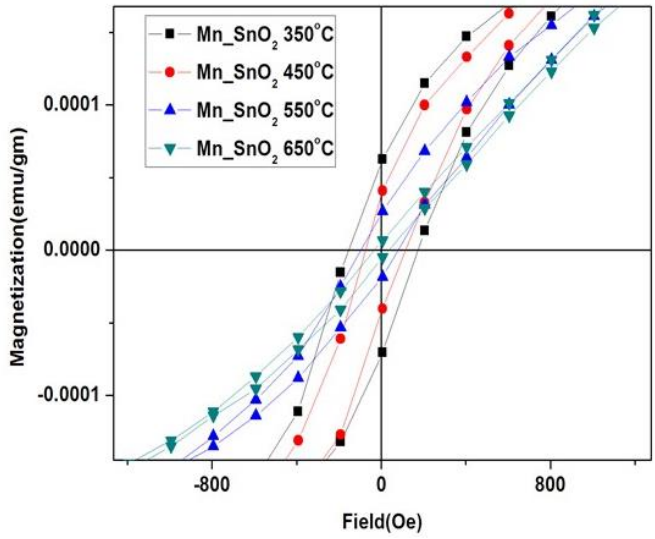

Fig. 5. Magnified M-H magnetization curves for nanocrystalline Mn- doped SnO_2 samples annealed at 350, 450, 550 and 650 ^oC.

This may be ascribed to the reason that the F-centre electron that occupies the d shell of Mn atom coupled with the Mn ion spin states becomes antiparallel giving rise to antiferromagnetic coupling thereby lowering the saturation magnetization. This might be because of quantum confinement effect in particle size which arises due to increasing annealing temperature. Fig. 5 shows the magnified magnetic measurements of Mn-doped SnO_2 samples annealed at different annealing temperatures. It suggests that increasing the annealing temperature diminishes the width of the ferromagnetic loop. This can be

explained that as the annealing temperature increases, the ferromagnetic ordering as well as the coercive field decreases, indicating a crucial phase transformation from ferromagnetism to paramagnetism. This phase transformation might be due to lesser direct and indirect exchange interactions which might arise because of diffusion of dopant ions which cause distortion in the crystal lattice at higher annealing temperatures [1].

3.3. *Optical investigations*

The confirmation of Mn ion substitution in SnO_2 lattice has been obtained from UV-Vis-NIR spectroscopy. In Fig. 6 a sharp absorption edge has been observed for pristine SnO_2 annealed at 350 °C at 284 nm. With Mn-doping a slight shift in the absorption edge has been observed for 350 °C (291 nm), 450 °C (295 nm), 550 °C (299 nm) and 650 °C (306 nm) indicating shifting of absorption peak towards higher wavelength. For Mn-doped SnO_2 samples annealed at 350 °C, the absorption peak decreases slightly. But as the annealing temperature increases, particle size increases and a red shift in absorption edges as well as increase in absorption has been observed for the samples annealed at 450, 550 and 650 °C.

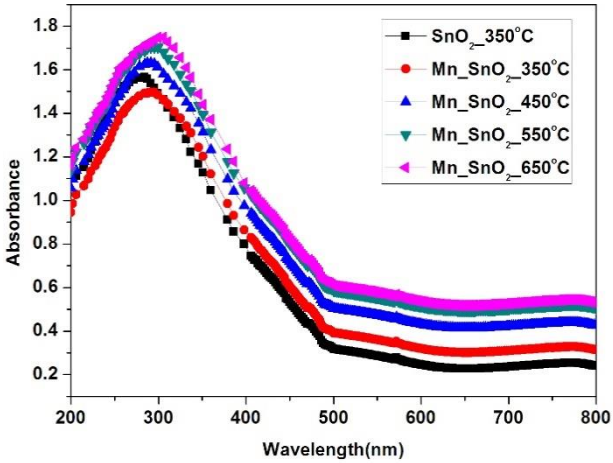

Fig. 6. Absorbance spectrum of pristine SnO_2 annealed at 350 °C and nanocrystalline Mn-doped SnO_2 samples annealed at 350, 450, 550 and 650 °C.

In UV-Vis spectroscopy, absorption coefficient α is obtained from Beer Lambert's law. According to this law

$$\alpha=2.303(A/L) \quad (3)$$

Absorbance is related to incident intensity I_o and transmitted intensity I by relation

$$A= log\ (I_o/ I) \quad (4)$$

Finally, Tauc's relation was used to determine the optical band gap, E_g, of Mn-doped SnO_2 samples in Eq (5). [41]:

$$\alpha h\nu = A\,(h\nu - E_g)^{1/2} \tag{5}$$

where α is the absorption coefficient, A^* isa constant, $(h\nu)$ is the photon energy and E_g is the energy band gap. The variation in $(\alpha h\nu)^2$ with $h\nu$ is observed for the $Sn_{1-x}Mn_xO_2$ samples in Fig. 7.

The linear portion of plot $(\alpha h\nu)^2$ versus $(h\nu)$ is extrapolated to intercept the photon energy values to obtain the energy band gap. The $(\alpha h\nu)^2$ versus $h\nu$ curve gives direct optical band gap for Mn-doped SnO_2 samples since the plot asymptotically tend towards a linear portion. The measured band gap for pristine SnO_2 sample was found to be 3.05 eV. The measured band gap value is thus smaller than the value of bulk SnO_2 (3.6 eV) reported. This might be due to the quantum confinement effect.

The calculated E_g values are given in Table 3 which shows that the band gap decreases as the particle size increases with increase in annealing temperature. Various factors like oxygen deficiency, impurity centres, surface roughness etc. may be attributed for the change in absorbance spectra. It has been understood from the local density approximation (LDA) [42] that the defects caused by Sn interstitial sites are mainly responsible for conduction than oxygen vacancies in pristine SnO_2. It is assumed that due to loosely bound outer electrons in interstitial sites of Sn, a new donor level is created in the conduction band.

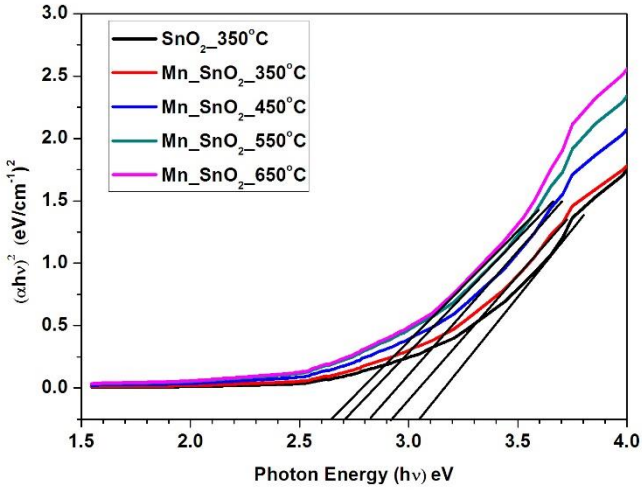

Fig. 7. Plot of $(\alpha h\nu)^2$ vs. photon energy of pristine SnO_2annealed at 350 °C and nanocrystalline Mn-doped SnO_2 samples annealed at 350, 450, 550 and 650 °C.

Table 3. Band Gap (E_g) values of Mn-doped SnO_2 samples at different annealing temperatures.

Sample name	Crystallite size (nm)	Band gap (E_g) eV
SnO_2_350 °C	35.00	3.05
Mn_SnO_2_350 °C	19.52	2.91
Mn_SnO_2_450 °C	33.00	2.82
Mn_SnO_2_550 °C	34.50	2.71
Mn_SnO_2_650 °C	34.50	2.62

On the other hand, oxygen vacancies are produced in the band gap. But the presence of Sn interstitial sites in the conduction band supresses the formation of oxygen vacancies. This decreases the inter-conduction band absorption in SnO_2 leading to large band gap that inhibits transitions in the visible region. Mn-doping leads to modification in conduction bands due to surface diffusion of Mn ions and Mn d-state orbitals into the band gap. This leads to overlapping of functions leading to change in band gap. A red shift is observed in band edges of Mn-doped SnO_2 in comparison to pristine SnO_2. This observation cannot be explained with quantum confinement phenomenon normally. It is assumed that band gap renormalization effect might be responsible for the red shift of the band edge due to doping. With increase in annealing temperature, particle size increases which leads to more diffusion of Mn ions and Mn d-state orbitals, thereby declining the band gap. Actually with Mn-doping, there are interactions due to sp-d exchange between the band electrons of the host (Sn^{4+}) and d electrons of the dopant (Mn^{4+}). This leads to change in the edges of the conduction and valence bands resulting into narrowing of band gap.

4. Conclusion

Summarizing, pristine SnO_2 and Mn-doped SnO_2 samples have been chemically synthesized by co-precipitation technique with low Mn concentration (2 %) at different annealing temperatures 350, 450, 550 and 650 °C. It was observed from the XRD data that though the crystallite size decreases with introduction of Mn dopant but with increasing annealing temperature, the crystallite size increases. Morphological and compositional formation of Mn-doped SnO_2 samples were examined by SEM and EDX respectively. Magnetic investigations show typical ferromagnetic ordering (magnetic saturation) for Mn- doped SnO_2 samples. On increasing the annealing temperature, saturation magnetization decreases at high magnetic field due to antiferromagnetic coupling. The width of the ferromagnetic loop shows a phase transformation from ferromagnetism to paramagnetism due to distortion in the crystal lattice with diffusion of dopant ions at higher annealing temperature. A red shift is observed in the band edges of Mn-doped SnO_2 samples due to band gap renormalization effect resulting into narrowing of band gap. From the results it was concluded that annealing temperature plays a major factor in the magnetic and optical properties of Mn-doped SnO_2 samples.

References

1. N. Ahmad, S. Khan, and M. M. N. Ansari, Physica B: Cond. Matt. **558**, 131 (2019). https://doi.org/10.1016/j.physb.2019.01.044
2. W. Prellier, A. Fouchet, and B. Mercey, J. Phys: Cond. Matt. **15**, R1583 (2003). https://doi.org/10.1088/0953-8984/15/37/R01
3. J. M. D. Coey, M. Venkatesan, and C. B. Fitzgerald, Nature Material **4**, 173 (2005). https://doi.org/10.1038/nmat1310
4. M. Sabarilakshmi and K. Janaki, Int. J. Sci. Res. **7**, 220 (2018).
5. T. P. Wai, Y. Yin, X. Zhang, and Z. Li, J. Nanomat. **2020**, 1 (2020). https://doi.org/10.1155/2020/8958043
6. G. Faglia, C. Baratto, G. Sberveglieri, M. Zha, and A. Zappettini, Appl. Phys. Lett. **86**, ID 011923 (2005). https://doi.org/10.1063/1.1849832
7. Y. Wang and J. Y. Lee, J. Phys. Chem. B, **108**, 1783 (2004). https://doi.org/10.1021/jp048904k
8. N. Q. Jia, Q. Zhou, L. Liu, M. M. Yan, and Z. Y. Jiang, J. Electroanal. Chem. **580**, 213 (2005). https://doi.org/10.1016/j.jelechem.2005.03.029
9. S. Mehraj, M. S. Ansari, and Alimuddin, Thin Solid Films **589**, 57 (2015). https://doi.org/10.1016/j.tsf.2015.04.065
10. H. Sugimoto, H. Tsukube, and K. Tanaka, Eur. J. Inorg. Chem. **23**, 4550 (2004). https://doi.org/10.1002/ejic.200400546
11. H. Zhang, D. Wang, C. Hu, X. Kang, and H. Liu, Actuators B Chem. **184**, 288 (2013). https://doi.org/10.1016/j.snb.2013.04.085
12. A. I. Ayesh, S. T. Mahmoud, S. J. Ahmad, and Y. Haik, Mater. Lett. **128**, 354 (2014). https://doi.org/10.1016/j.matlet.2014.04.173
13. H. Tang, Q. Cao, Z. He, S. Wang, J. Han, T. Li, B. Gao, J. Yang, D. Deng, and X. Li, Sol. RRL **2020**, 4 (2019). https://doi.org/10.1002/solr.201900415
14. K. S. Reddy, S. Nithiyanantham, G. Geetha, R. A. Sujatha, S. Mahalakshmi, J. Mat. Appl. **8**, 1 (2019).
15. N. Ahmad, S. Khan, and M. M. N. Ansari, Mater. Res. Express **5**, ID 035045 (2018). https://doi.org/10.1088/2053-1591/aab5a3
16. E. T. Selvi and S. M. Sunder, J. Mat. Sci: Mat. Elect. **28**, 15021 (2017).
17. A. Ahmed, T. Ali, M. N. Siddique, A. Ahmed, and P. Tripathi, J. Appl. Phy. **122**, ID 083906 (2017). https://doi.org/10.1063/1.4999830
18. N. Salah, S. Habib, A. Azam, M. Shahnawaze, and W. M. Al-Shawafi, Nanomater. Nanotechnol. **6**, 17 (2016). https://doi.org/10.5772/62520
19. V. S. Anitha, S. Sujatha, and L. K. Joy, J. Alloy. Comp. **675**, 331 (2016). https://doi.org/10.1016/j.jallcom.2016.03.045
20. K. Srinivas, M. Vithal, B. Sreedhar, M. M. Raja, and P. V. Reddy, J. Phys. Chem. C, **113**, 3543 (2009).https://doi.org/10.1021/jp809146x
21. A. Gupta, H. Cao, K. Parekh, K. Rao, A. Raju, and U. Waghmare, J. Appl. Phys. **101**, 513 (2007). https://doi.org/10.1063/1.2712018
22. D. P. Rai, A. Laref, A. Shankar, A. P. Sakhya, R. Khenata, and R. K. Thapa, J. Phys. Chem. Solids **120**, 104 (2018). https://doi.org/10.1016/j.jpcs.2018.04.006
23. K. Joy, S. S. Lekshmy, P. B. Nair, and G. P. Daniel, J. Alloy. Compd. **512**, 149 (2012). https://doi.org/10.1016/j.jallcom.2011.09.051
24. X. L. Wang, Z. X. Dai, and Z. Zeng, J. Phys. Cond. Matt. **20**, ID 045214 (2008). https://doi.org/10.1088/0953-8984/20/04/045214
25. X. F. Liu and R. H. Yu, J. Appl. Phys. **102**, ID 083917 (2007). https://doi.org/10.1063/1.2801375
26. C. B. Fitzgerald, M. Venkatesan, A. P. Douvalis, S. Huber, and J. M. D. Coey, J. Appl. Phys. **95**, 7390 (2004). https://doi.org/10.1063/1.1676026
27. S. B. Ogale, R. J. Chodhary, J. Buban, and S. E. Lofland, Phy. Rev. Lett. **91**, ID 077205 (2003). https://doi.org/10.1103/PhysRevLett.91.077205

28. J. Zhang, Q. Yun, and Q. Wang, Modern Appl. Sci. **4**, 124 (2010). https://doi.org/10.5539/mas.v4n11p124
29. J. Hays, A. Punnoose, R. Baldner, M. H. Engelhard, J. Peloquin, and K. M. Reddy, Phys. Rev. B,**72**, ID 075203 (2005). https://doi.org/10.1103/PhysRevB.72.075203
30. C. Steven, L. Z. Erwin, I. H. Michael, L. E. Alexander, A. K. Thomas, and J. N. David, Nature **436**, 91 (2005).
31. M. SaravanaKumar, S. Agilan, N. M. K. Samy, V. Rukkumani, A. Marusami, and A. Ranjitha, Acta Physics Polonica A **127**, 1656 (2015). https://doi.org/10.12693/APhysPolA.127.1656
32. A. Azam, A. A. Ahmed, S. S. Habib, and A. H. Naqvi, J. Alloy. Comp. **523**, 83 (2012). https://doi.org/10.1016/j.jallcom.2012.01.072
33. R. Viswanatha, Parmana-J. Phys. **84**, 1055 (2015). https://doi.org/10.1007/s12043-015-1001-0
34. Y. Wei, J. Liu, F. Cheng, and J. Chen, J. Mat. Sci. A **34**, 1 (2019).
35. S. Sabri, M. S. M. Deni, A. Zakaria, and M. K. Talari, Phys. Proc. **25**, 233 (2012). https://doi.org/10.1016/j.phpro.2012.03.077
36. M. M. Bagheri-Mohagheghi and M. Shokooh-Saremi, Semiconductor Sci. Technol. **19**, 764 (2004). https://doi.org/10.1088/0268-1242/19/6/019
37. Z. M. Tian, S. L. Yuan, J. H. He, P. Li, S. Q. Zhang, C. H. Wang, Y. Q. Wang, S. Y. Yin, and L. Liu, J. Alloys Compd. **466**, 26 (2008). https://doi.org/10.1016/j.jallcom.2007.11.054
38. B. D. Cullity and S. R. Stock, Elements of X-ray Diffraction, 3rd Edition (Prentice Hall, Upper Saddle River, 2001).
39. W. Gopel and K. D. Schierbaum, Sensor and Actuator B-Chem. **26**, 1 (1995). https://doi.org/10.1016/0925-4005(94)01546-T
40. K. Nomura, J. Okabayashi, K. Okamura, and Y. Yamada, J. Appl. Phys. **110**, 083901(2011). https://doi.org/10.1063/1.3651468
41. D. L. Wood and J. Tauc, Phys. Rev. B **5**, 3144 (1972). https://doi.org/10.1103/PhysRevB.5.3144
42. K. Cetin and A. Zunger, Phys. Rev. Lett. **88**, ID 095501 **(**2002).